PAPER

Check for updates

Naproxen release from carbon dot coated magnetite nanohybrid as versatile theranostics for HeLa cancer cells†

Mochamad Z. Fahmi, [ID] *[ab] Nurlailiatul Machmudah,[a] Putri Indrawasih,[a] Aswandi Wibrianto, [ID] [ac] Musbahu A. Ahmad, [ID] [a] Satya C. W. Sakti[ab] and Jia-yaw Chang[c]

Nanohybrid magnetite carbon dots (Fe_3O_4@CDs) were successfully synthesized to improve their applicability in multi-response bioimaging. The nanohybrid was prepared *via* pyrolysis and further loaded with naproxen (NAP) to promote drug delivery features. The characterization of the synthesized Fe_3O_4@CDs demonstrated the existence of Fe_3O_4 crystals by matching with JCPDS 75-0033 and its narrow size distribution at 11.30 nm; further, FTIR spectra confirmed the presence of Fe–O groups, C–O stretching, C–H sp^2, and C–O bending, along with dual-active fluorescence and magnetic responses. The nanohybrids also exhibit particular properties such as a maximum wavelength of 230.5 nm, maximum emission in the 320–420 nm range, and slight superparamagnetic reduction (Fe_3O_4: 0.93620 emu per g; Fe_3O_4@CDs: 0.64784 emu per g). The cytotoxicity assessment of the nanohybrid revealed an excellent half-maximal inhibitory concentration (IC_{50}) of 17 671.5 ± 1742.6 μg mL^{-1}. Then, the incorporation of NAP decreased the cell viability to below 10%. The kinetic release properties of NAP are also confirmed as pH-dependent, and they follow the Korsmeyer–Peppas kinetics model. These results indicated that the proposed Fe_3O_4@CDs can be used as a new model for theranostic treatment.

Introduction

Inorganic-based nanomaterials including magnetic nanoparticles (MNPs) and carbon dots (CDs) have been increasingly studied owing to their unique optical, electrical, and magnetic properties.[3] Magnetite (Fe_3O_4)-based MNPs are particularly interesting due to their superior physical properties including biodegradability, biocompatibility, and superparamagnetism. The material distorts human tissue's local magnetic characteristics to enhance image contrast. Fe_3O_4 has thus gained interest both in the field of magnetic storage and in biomedical areas including biosensor development,[5] hyperthermia therapy,[6] drug delivery,[7] medical imaging,[8] clinical diagnoses,[9] cardiovascular therapy,[10] and magnetic separation.[11]

Several studies reported the application of Fe_3O_4-based MNPs for clinical use as a contrast agent in magnetic resonance imaging (MRI).[12,13] The current MRI contrast agents mostly form Gd-based molecules and remain at a high risk of toxicity due to their long-term existence in the human body without systemic degradation. However, Fe_3O_4-based MNPs stand as better alternatives due to their high-level acceptance in the human body (about 20–25 mg), which is similar to the amount of contrast agent injected per person (0.5 mg kg^{-1}). This reason spurs many studies on obtaining MNPs by various methods including hydrothermal, solvothermal, electrochemical, and sonochemical methods and co-precipitation, microemulsion, sol–gel, and thermal decomposition.[14–20] Among all methods, co-precipitation is a promising method that allows for short preparation time, low-cost precursors, and low-temperature processing.[21,22] However, colloidal Fe_3O_4-based MNPs tend to agglomerate in water due to high surface energy and magnetic dipole–dipole attraction between crystals.[3,23] Surface modification can enhance their colloidal water stability, which also influences their biodistribution and bloodstream circulation.[24] The proposed methods have been reported to involve modification or coating of the surface of Fe_3O_4 with carboxylates, sulphonates, gold, phosphates, silicon compounds, polymers, and CDs. Thus, the modifications are also responsible to reduce its hydrodynamic size and improve its stability in water.[13,25,26] It is known from previous studies the carboxylate moiety of citric acid (CA) has been widely used as a stabilizing agent to bind to

a Department of Chemistry, Universitas Airlangga, Surabaya 61115, Indonesia

b Supra Modification Nano-Micro Engineering Research Group, Universitas Airlangga, Surabaya 60115, Indonesia

c Department of Chemical Engineering, National Taiwan University of Science and Technology, Taipei 10607, Taiwan, ROC. E-mail: m.zakki.fahmi@fst.unair.ac.id; Fax: +62-31-5922427; Tel: +62-31-5922427

the surface of MNPs and increase the negative charge and hydrophilicity.[22,25,27,28]

However, CDs have also attracted attention as a promising material for numerous applications such as photocatalysis, metal detection, drug delivery, bioimaging, bio-labelling, biosensing, and light-emitting diodes or optoelectronic devices due to their photoluminescence (PL).[29–31] Further, their luminescence offers good cell-imaging qualities including long-term cell tracking, deep-tissue penetration when excited at longer wavelengths, and better resistance against photo-bleaching than fluorescent dyes.[27,32] The commonly used CDs have been synthesized by top–down and bottom–up approaches including laser ablation, microwave radiation, hydrothermal/solvothermal methods, thermal decomposition, and pyrolysis.[6,33–36] Focusing on CD synthesis, it was reported that the process could support the nucleation and growth stages of other NPs, leading to new functional materials. Thus, CDs play a critical role in preventing the agglomeration of composite materials.[37] CDs synthesized from CA are favourable, which demonstrated the enhancement of magnetic compatibility with solvents, reduced aggregate formation, and increased NP stability; importantly, these water-soluble CDs have shown high PL with a quantum yield (QY) of approximately 42.2–88.6%.[32,38,39]

Combining CDs and MNPs as hybrid NPs allows multi-purpose nanomaterials in their applications.[34,40] Several studies have thus investigated nanohybrids comprising MNPs and CDs in diverse fields such as catalysis, sensing, fuel cell technology, optoelectronics, magnetism, energy, and biomedicine.[37,41] Some efforts have been focused on preparing novel hybrids comprising CDs with inorganic NP cores such as iron oxide, zinc oxide, or silica. Singh *et al.*[42] have successfully synthesized magnetic quantum dot Fe_3O_4–ZnO nanohybrids that targeted cancer cells. Moreover, BSA-modified hybrid nanoclusters have been synthesized to improve the response during magneto-fluorescence imaging and drug delivery.[41] However, each imaging modality has its advantages and disadvantages. Multi-modal imaging techniques combine each modality's strengths and further improve diagnostic techniques to be developed on reaching the effectiveness of diagnostic protocols.[43,44] For instance, magnetic resonance imaging (MRI), owing to less sensitivity, could be combined with compassionate modalities like computer tomography (CT). The combination of CDs covering MNPs promotes advantages based no toxicity issue and could be used in drug delivery systems.

In case of delivery systems upon nanocarriers, a study on the releasing character of the drug may be a crucial aspect to support desired therapy technique. Nevertheless, most of the hybrid materials are reported without any details on how they carry drugs to the target site, and are prepared *via* complicated processes along with the costly design. Some studies have reported the combination of CDs and Fe_3O_4 nanohybrids, which exhibit superior and multi-functional features on detecting particular compounds such as doxycycline,[45] *Geobacter sulfurreducens*,[46] bacteria,[47] and metals.[47,48] However, integrative studies on the evaluation of naproxen release from the nanohybrid and its potential delivery have not been reported yet. In present research, we propose simple *in situ* synthesis of a nanohybrid of Fe_3O_4 NPs conjugated with CDs. The nanohybrid further loaded with naproxen (NAP) is used as a nonsteroidal anti-inflammatory drug, as it is commonly used as a modifying adjunct during healing.[49,50] The proposed nanohybrid comprising both Fe_3O_4-based MNPs and CDs and thus incorporating both of their functionalities in a single NP is very promising for multi-response bioimaging such as MRI and CT.

Experimental

Materials

Iron (III) chloride (97%; $FeCl_3$), ammonium iron (II) sulphate (99.97%; $(NH_4)_2Fe(SO_4)_2 \cdot 6H_2O$), ammonium hydroxide (25%; NH_4OH), ethanol (99.5%; C_2H_5OH), Na-NAP (98%), and $4',6$-diamidine-2'-phenylindole dihydrochloride (DAPI) were purchased from Sigma-Aldrich, USA. CA (99.5%; $C_6H_8O_7$) and hydrochloric acid (37%; HCl) were purchased from Merck, Germany. Dulbecco's modified Eagle's cell medium and phosphate buffered saline (PBS) were purchased from GIBCO Thermo Scientific, USA. A molecular weight cut-off (MWCO) membrane (1000 Da) was purchased from Orange Scientifique, Belgium. All chemicals were used directly without further purification.

Synthesis of Fe_3O_4@CA and Fe_3O_4@CDs

Fe_3O_4@CA was prepared following the procedure previously reported in the literature with slight modification.[51,52] First, 8.1 g of $FeCl_3$ and 9.8 g of Mohr's salt were dissolved in 25 mL of deionized (DI) water and added to 20 mL of ammonia under vigorous stirring. The mixture was then subjected to ultrasonication for 30 min until the pH reached 9 and then stirred vigorously at 70 °C for 30 min. The resulting black mixture was separated by centrifugation (900 rpm) and washed with DI water and ethanol. The obtained Fe_3O_4 was added to 100 mL of DI water, stirred and ultrasonicated for 30 minutes. Once reaching pH = 5, the mixture was stirred at 80 °C for 1 h to obtain nano-Fe_3O_4.

Next, 15 g L^{-1} of CA was added to the mixture at a rate of 2 mL min^{-1} for 30 min. The resulting black mixture was separated by centrifugation (900 rpm) and washed with DI water. The black precipitate of Fe_3O_4@CA NPs was collected and added to more CA (ratio 1 : 1) and furnaced at 270 °C for 1 h to obtain the Fe_3O_4@CDs nanohybrid. The colloidal solution was then prepared by dissolving the resulting nanohybrid in 1 M sodium hydroxide (NaOH) and then purifying it on a dialysis membrane (MWCO; 1000 Da) for 2 h.

Preparation of NAP-loaded Fe_3O_4@CDs and drug release assessment

NAP-loaded Fe_3O_4@CDs (Fe_3O_4@CDs -NAP) were prepared by mixing the NAP solution with Fe_3O_4@CDs at a molar ratio of 1 : 10 at room temperature and stirring for 24 h. Fe_3O_4@CDs-NAP were then dialyzed using an MWCO 1000 Da membrane for 24 h to remove impurities. The NAP concentration contained in the Fe_3O_4@CDs-NAP was calculated by matching the maximum

absorbance of NAP with the original standard curve at 330.5 nm.[53]

Confocal laser scanning investigation

This observation was started by culturing HeLa cells, which were first seeded in a 6-well plate containing a culturing medium (2 mL) and cultured for 24 h. After incubating with the sample (300 μL) for 60 min, the cells were washed three times with a PBS solution and then fixed with 70% alcohol for 10 min. Fluorescence images of HeLa cells were acquired using a Leica TCS SP2 inverted confocal microscope (Leica Microsystems) equipped with a 63 ×1.32 NA oil immersion objective. Confocal images were obtained by illuminating the samples with inline Ar (488 nm) and He–Ne (503–680 nm and 588 nm) lasers.

Cytotoxicity evaluation of Fe_3O_4@CDs and drug inhibition assessment

A cytotoxicity assessment was performed using a Cell Counting Kit-8 (CCK-8) from MedChemExpress, New Jersey, USA, in a 96-well plate for HeLa cancer cell lines. The cancer cell lines were cultured in Dulbecco's modified Eagle's medium (DMEM) at a density of 250 000 cells per well and incubated for 24 h. Then, the cells were washed with 10 μL of phosphate and different concentrations of Fe_3O_4 @CDs were added. After that, the medium was allowed to equilibrate for 1 h. The contents of each well were then added to 20 μL of the CCK-8 reagent at 37 °C in a humidified 5% CO_2 atmosphere. Finally, the absorbance of each sample at 480 nm was recorded using an enzyme-linked immunosorbent assay (ELISA) reader.

Characterization

The particle size was measured using a dynamic light scattering (DLS) instrument Malvern Zetasizer and an atomic force microscope (AFM). Then, the diameter size distribution was obtained using the ImageJ software. The functional groups of the NPs were studied using a Shimadzu IR-Tracer-100 Fourier-transform infrared spectrometer (FTIR). X-ray powder diffraction (XRD) patterns were acquired using a Phillips X-ray diffractometer with a Cu-Kα line (λ = 1.54 Å). Ultraviolet-visible spectrophotometry (UV-vis) absorption spectra were recorded using a Shimadzu 1800 UV-vis spectrophotometer. PL spectra were recorded using a FluoroMax-4 PL spectrophotometer equipped with a xenon lamp. The QY of Fe_3O_4@CDs was compared with that of Rhodamine 6G (R6G, QY = 95%) and calculated as follows:[54]
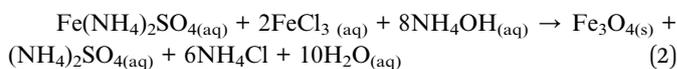
$$QY = QY_r \, (I_s/I_r) \, (A_r/A_s) \, (\eta_s/\eta_r)^2 \tag{1}$$

where I, A, and η correspond to the PL intensity, UV absorbance, and refractive index, respectively. Subscripts r and s represent the Fe_3O_4@CDs and R6G markers, respectively. The magnetic properties of the NPs were measured at room temperature using a vibrating-sample magnetometer (VSM) with a maximum applied field of 8 kG.

Results and discussion

### Synthesis and characterization of the nanohybrid

For preparing magnetite nanoparticles, we first prepared bulk magnetite (Fe_3O_4) by mixing the ionic iron sources by a co-precipitation method following reaction eqn (2):

$$Fe(NH_4)_2SO_{4(aq)} + 2FeCl_{3\,(aq)} + 8NH_4OH_{(aq)} \rightarrow Fe_3O_{4(s)} + (NH_4)_2SO_{4(aq)} + 6NH_4Cl + 10H_2O_{(aq)} \tag{2}$$

The obtained magnetite further was introduced to CA to cover the magnetite and enhance its stability. As shown in Scheme 1, the carboxylate moieties of CA stabilize the magnetite *via* temporary complex formation and the rest of carboxylates promote Fe_3O_4 for further reaction.[55] The interaction between CA and magnetite was mediated *via* electrostatic interaction from the carboxylate moieties of CA close to the iron part of magnetite. This design not only covers magnetite itself, but also stabilizes the particle. The CA to iron interaction may rob the iron oxide particle, resulting in a lower diameter of magnetite after introducing CA (next on size-diameter discussion). This CA-coated magnetite was further treated *via* pyrolysis after the addition of excess CA. The pyrolysis process allows carbonation of CA in between. In this process, any hydroxy moieties on CA can interact with hydrogen or other hydroxy spices, covering magnetite and obtaining a carbon-like structure of carbon dots covering magnetite (Fe_3O_4@CDs) as a new layer, as detailed in Scheme 1. The produced nanomaterial was studied by several characterizations. The carbon precursor on the outer layer of Fe_3O_4 enhanced its PL and increased its stability in water. CDs have been demonstrated to enhance the PL and stability of NPs,[31] and the hydrophilic material can be more easily absorbed in the human body for clinical application and prevent side effects.[56] To prove the above-mentioned statement, some characterizations were performed in the present study.

DLS was applied to first determine the obtained samples, which were dispersed in water, as shown in Fig. 1a. The size distribution data showed that Fe_3O_4 (I) had the biggest average particle size distribution, up to 1814 nm; this phenomena proved that the obtained Fe_3O_4 particles synthesized by co-precipitation are seemingly unstable and tend to agglomerate in water.[3,23] Introducing CA on the magnetite (to perform Fe_3O_4@CA) drives down its average particle diameter to 1221 nm. The size lowering was due to the coating of CA's functional groups onto Fe_3O_4, preventing it to from agglomerating, thereby increasing its hydrodynamic stability and decreasing the particle size. Moreover, the nanohybrid Fe_3O_4@CDs reached the smallest average particle size (up to 198.8 nm). These phenomena showed that the abundance of CA's functional groups can be optimized to prevent Fe_3O_4 aggregation and form CDs as stabile coating structures. Next, the AFM images visualise the topography of Fe_3O_4@CDs, where the height of Fe_3O_4@CDs was measured to be 10 nm to 35 nm, as shown in Fig. 1b and c. The size distribution of Fe_3O_4@CD particles was calculated using a Gaussian equation on the Origin software. As shown in Fig. 1d, the Fe_3O_4@CDs were 18.2 ± 0.3 nm in diameter, which support the previous data
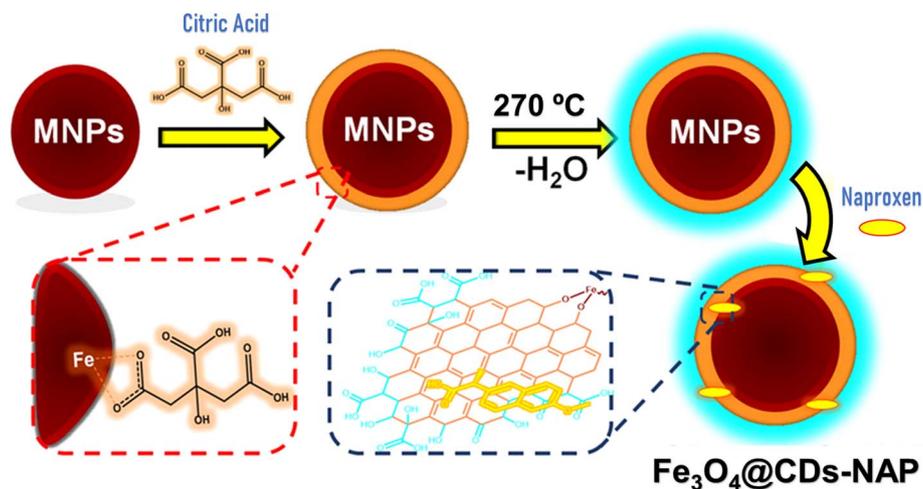
Scheme 1 Schematic route for developing nanohybrid naproxen-loaded magnetite carbon dots (Fe₃O₄@CDs-NAP).

confirming that Fe_3O_4@CDs have a smaller size than that of bare Fe_3O_4. These data also revealed the effectiveness of CA on covering the magnetite well and the capability of degrading the Fe_3O_4 size.[57] For supporting the AFM data, the TEM observation was further conjugated to the nanohybrid (Fig. 2). TEM also confirms that addition of CDs may reduce Fe_3O_4 size form above 25 nm (Fe_3O_4) to below 25 nm (Fe_3O_4@CDs), on average. This finding also reveals that the incorporation of CDs onto magnetite reduces the aggregation potency that can be further advantageous for applications. With regard to the previous report on the use of nanomaterials for endocytosis and controlled drug release process, Fe_3O_4 is generally less than 345 nm in diameter;[58,59] the finding of the size of Fe_3O_4@CDs may strengthen the potential application of the nanohybrid in biomedical fields.

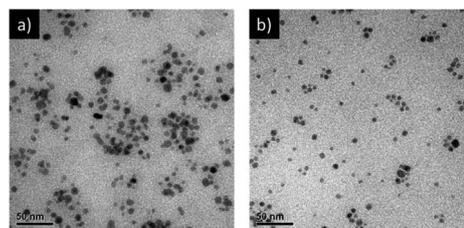The crystal structures of Fe_3O_4, Fe_3O_4@CA, and Fe_3O_4@CDs were then compared *via* XRD observation, where the patterns fit

Fig. 2 TEM images of Fe_3O_4 (a) and Fe_3O_4@CDs (b). The bars represent 50 nm.

with JCPDS 75-0033, confirming the existence of magnetite structures on nanohybrids (shown in Fig. 3). In detail, all samples showed similar Miller indices of Fe_3O_4 on (220), (311), (222), (311), (400), (511), and (440) planes. By using the Scherrer equation, the crystal diameter of the Fe_3O_4, CA@Fe_3O_4 and Fe_3O_4@CDs were confirmed to be 3.79, 3.78, and 3.09 nm, respectively. These findings also support the previous results that the size of magnetite decreases once it is conjugated with CA. This makes it suitable for possible therapeutic applications because materials less than 100 nm in diameter have favourable biodistribution and clearance/accumulation behaviour in the human body.[25]

Subsequently, absorption and emission of Fe_3O_4@CDs were monitored by UV-vis and PL spectrophotometry. From both assessments, it was confirmed that the produced Fe_3O_4@CDs had a maximum absorbance at 230.5 nm, indicating the $\pi \rightarrow \pi^*$ electron transition of the C=C bond in the CD core.[31] Additionally, a shoulder peak was present at 329 nm, which demonstrates the $n \rightarrow \pi^*$ electron transition of the carbonyl group (Fig. 4a).[1] The emission spectrum of Fe_3O_4@CDs at 410 nm is displayed in Fig. 4b; the spectra showed blue fluorescence with red-shifted emission and excitation wavelengths, as the excitation wavelength was increased.[60,61] To attain significant improvement in spectrophotometer observation, we next compared the absorbance of bare magnetite, Fe_3O_4@CA and the Fe_3O_4@CDs (Fig. S1, ESI†), and the nanohybrid showed
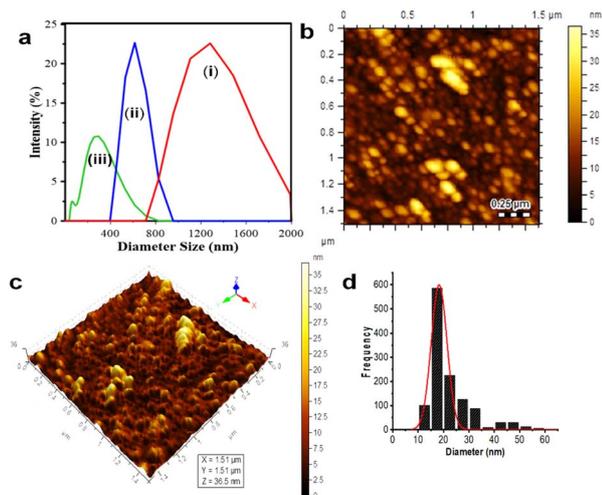

Fig. 1 (a) Dynamic light scattering (DLS) particle diameter distribution: (i) Fe_3O_4; (ii) citric-acid-coated Fe_3O_4 (Fe_3O_4@CA); and (iii) Fe_3O_4@CDs. (b) 2D and (c) 3D morphology of Fe_3O_4@CDs. (d) Size distribution.
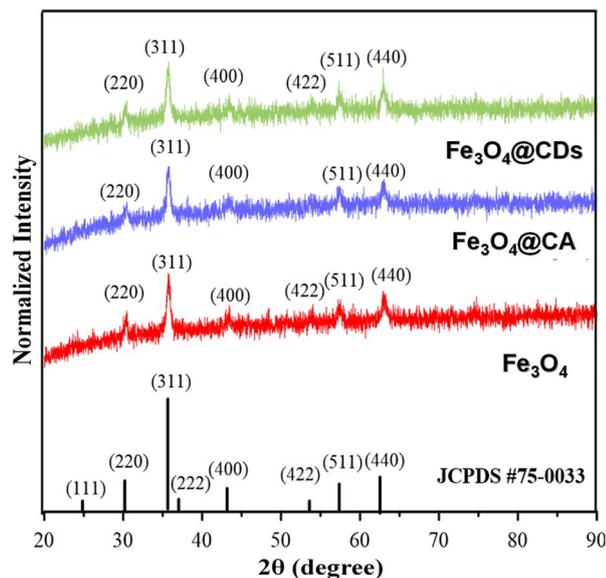
Fig. 3 X-ray diffraction (XRD) patterns of pure magnetite (red), Fe$_3$O$_4$@CA composite (blue), and Fe$_3$O$_4$@CDs (green), verified with Fe$_3$O$_4$ JCPDS database.

several absorption peaks at significantly higher emission compared to the bare magnetite and Fe$_3$O$_4$@CA. This finding proved the attachment of CDs on the surface of magnetite with chemical binding. This interaction may happen, because CDs have shown good attraction with metal elements. Such property was even utilized for their use in metals.[62,63] Next, the QY percentage of the resulting Fe$_3$O$_4$@CDs reached up to 56.5%, where it was classified as a high QY among the reported metal-doped hybrid CDs, as detailed in Table 1. This finding confirms the good potency of the nanohybrid for use as a staining agent.

Functional group observation of the nanohybrid was done by FTIR to verify the surface modification of magnetite. The synthesized Fe$_3$O$_4$, Fe$_3$O$_4$@CA, Fe$_3$O$_4$@CDs, and Fe$_3$O$_4$@CDs-

NAP samples were examined at wavenumbers of 400–4000 cm^{-1}; the resulting spectra are shown in Fig. 4c. The 561–640 cm^{-1} band present in the synthesized Fe$_3$O$_4$ spectrum is associated with the Fe–O bonding of spinel ferrite.[64] Moreover, the broad bands at 3442 and 1629 cm^{-1} indicate the presence of O–H stretching and bending that occurs during co-precipitation, respectively. The spectrum of NAP showed several bands at 1680 and 1165 cm^{-1} that correspond to C=O and the C–O–C/methoxy groups contained in NAP, respectively. The band at 1589 cm^{-1} is present in the Fe$_3$O$_4$@CA spectrum, but not in that of Fe$_3$O$_4$@CDs associated with a C=C aromatic group, and thus, represents the dehydrogenation of CA forming graphene oxides during furnacing.[65] Finally, the generated band at 1135 cm^{-1} in the spectrum of the synthesized Fe$_3$O$_4$@CDs-NAP corresponds to the methoxy group of NAP, and thus, demonstrates the successful loading of NAP onto Fe$_3$O$_4$@CDs.

The measurement of the magnetic properties of samples was carried out using a VSM at room temperature at a magnetic field intensity of 8000–8000 Oe; the resulting saturation magnetization (M_s), remanent magnetization (M_r), and coercivity (H) are shown in Fig. 5. The resulting saturation magnetization of Fe$_3$O$_4$, Fe$_3$O$_4$@CA and Fe$_3$O$_4$@CDs was 80.569, 59.573, and 68.379 emu per g, respectively. The saturation magnetization of the synthesized materials was thus lower than that of Fe$_3$O$_4$ (92–100 emu per g) by a significant margin, thereby indicating that the sample was smaller than bulk Fe$_3$O$_4$. The saturation magnetization ratio for those samples compared with bulk Fe$_3$O$_4$ was 64.75%, 87.58%, and 74.33%, respectively. If the magnetization hysteresis curve is enlarged, the coercivity obtained from Fe$_3$O$_4$, Fe$_3$O$_4$@CA and Fe$_3$O$_4$@CDs was 25.462, 5.637 and 24.460 G, respectively, and the remanent magnetization was near zero: 2.679, 0.718 and 3.617 emu per g, respectively. The characteristic features of superparamagnetic include high saturation magnetization, low coercivity and remanent magnetization of zero when not influenced by an external magnetic field. The data derive an opinion that the
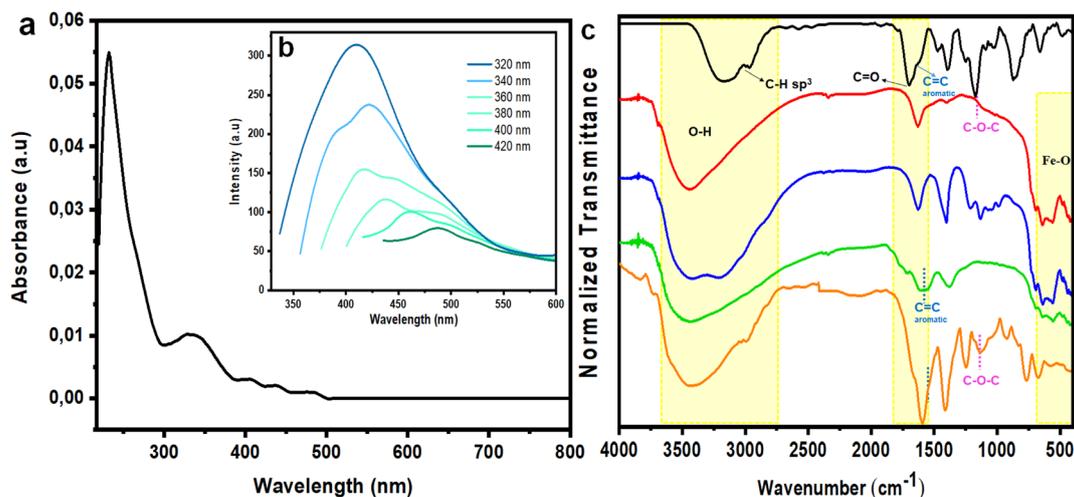

Fig. 4 (a) Ultraviolet (UV) spectrum and (b) PL intensity of Fe$_3$O$_4$@CDs with varied excitation wavelength (320–420 nm). (c) Infrared (IR) spectra of NAP (black), Fe$_3$O$_4$ (red), Fe$_3$O$_4$@CA (blue), Fe$_3$O$_4$@CDs (green), and Fe$_3$O$_4$@CDs-NAP (orange).

Table 1 Quantum yields (QY) of various metal carbon-based nanoparticles (NPs)

Precursor	Sample	Method	QY (%)	Ref
Citrate acid, ethanediamine	CQDs	Hydrothermal	48.32	1
Citrate acid, ethanediamine, $GdCl_3$	Gd-CQDs	Hydrothermal	31.78	
Citrate acid, ethanediamine, $GdCl_3$, $N–Fe_3O_4$	Gd-CQDs@$N–Fe_3O_4$	Solvothermal	1.29	
Black phosphorus, poly-lysine acid, ferric ammonium citrate, polyglutamic acid	GP-PGA-Fe_3O_4-CDs@BPQDs	Hydrothermal	6.8	2
Ferric ammonium citrate and triethylenetetramine	Fe_3O_4–CDs	Hydrothermal	4.8	4
Citrate acid, $FeCl_3$, $(NH_4)_2Fe(SO_4)_2 \cdot 6H_2O$	Fe_3O_4@CDs	Furnace-assisted	56.5	Present study
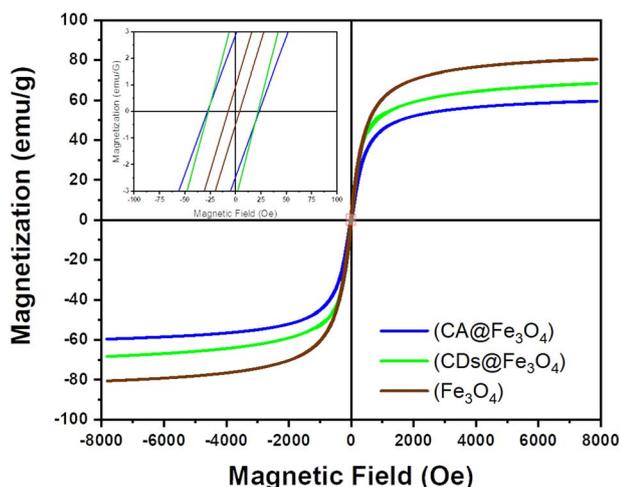
Fig. 5 Magnetization curve of Fe_3O_4, Fe_3O_4@CA, and Fe_3O_4@CDs.

addition of CA onto magnetite will diminish the magnetic properties due to the formation of huge amorphous regions on the surface of magnet; meanwhile, further carbonation of CA forming Fe_3O_4@CDs surprisingly enhances the magnetic properties. The emerged magnetic properties on the Fe_3O_4@-CDs could also be observed easily (Fig. S2, ESI†). Basically, formation of graphene-like structures on CDs is a responsible factor in increasing the magnetic properties, where the magnetic character emerged from the edge state of the graphene-like structure of CDs, resulting in dislocated energy within the pseudo gap.[66,67] These properties have only been demonstrated to appear for nano-sized materials and the ob-tained low remanent magnetization along with its coercivity value indicates that the three samples have superparamagnetic properties.[23,58]

In order to evaluate its use for biomedical application, the stability investigation of the nanohybrid is a crucial aspect that needs to be explored. We considered to assess the stability of Fe_3O_4@CDs against different pH values and ionic strength, where these two aspects are important regarding future studies *in vivo* and clinical administration on insertion of this nano-hybrid. We next use a turbidimeter for assessing any nano-hybrid degradation (Fig. S3, ESI†). The data illustrated that the nanohybrid exhibited low turbidity data in the pH range of 3–10, indicating good stability under that condition. Moreover,

the Fe_3O_4@CDs nanohybrid also showed good stability while it is against high–ionic strength condition (NaCl concentration up to 3 N). The good stability of the nanohybrid at different pH values and NaCl concentrations indicates the good potency of this nanomaterial in biomedical applications (normally at pH 7.4 and NaCl concentration at 0.15 N).

Cytotoxicity evaluation

The cytotoxicity of the Fe_3O_4@CDs against HeLa cancer cells after 24 h was assessed using the CCK-8 (Fig. 6). Even at a high concentration up to 600 μg mL^{-1}, the cell viability treated with Fe_3O_4@CDs is still maintained at a high percentage over 80%, which strongly demonstrates the high biocompatibility of the obtained Fe_3O_4@CDs. It is well known that CDs exhibited excellent biocompatibility and non-toxic features.[68] In the nanohybrid design, even Fe_3O_4 and other metal ferrites claimed also have low toxic effects;[52,53,69] CDs acting like a cover on the surface of magnetite nanoparticles would possibly prevent toxic reactions between the nanoparticles and the cellular system. Moreover, the half-maximal cytotoxic concentration (CC$_{50}$) of Fe_3O_4@CDs also supported this statement in proving the non-toxic property of the nanohybrid, even at a concentration as high as 17 671.5 ± 1742.6 μg mL^{-1} (showed on Fig. 7a). This finding also reveals that the CDs play an important role, not only in emerging optical properties, but also in their ability to cover
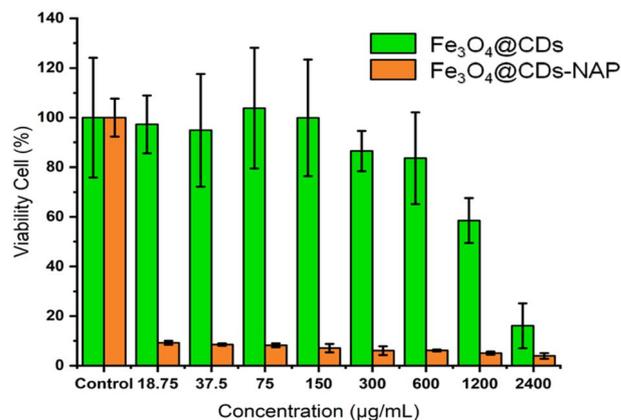

Fig. 6 Cell viability evaluation of HeLa cells by a CCK-8 assay after 24 h of incubation with Fe_3O_4@CDs (green) and Fe_3O_4@CDs-NAP (orange) compared with the negative control. All data are expressed as mean ± SD, $n = 5$.
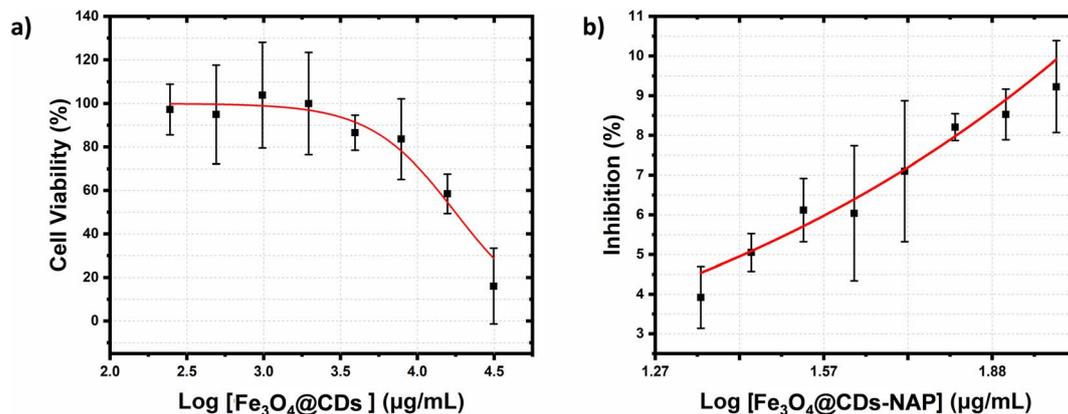
Fig. 7 HeLa cancer cell viability curves after 24 h incubation of (a) Fe₃O₄@CD nanohybrids and (b) inhibition of HeLa cancer cell curves after 24 h incubation of loaded Fe₃O₄@CDs-NAP nanohybrids. CC₅₀ and IC₅₀ values were plotted on the red fitted curves that resulted from dose-response mode on the Origin software. All data are expressed as mean ± SD with $n = 3$.

the magnetite nanoparticle and diminish the toxicity effect of the nanohybrid. The CC_{50} result of nanohybrid is also comparable with the other CD-based studies that claimed non-toxic nanomaterials (Table S1, ESI†). Furthermore, loading naproxen on the nanohybrid drives the cell viability percentage down significantly even at its low concentrations. The inhibited concentration (IC_{50}) of Fe₃O₄@CDs-NAP was 8.42 ± 1.09 µg mL⁻¹ (see Fig. 7b). Interestingly, this IC_{50} value was lower than that of naproxen itself (28.20 ± 1.09 µg mL⁻¹).[70] However, it is an intriguing observation regarding the ability of an anti-inflammatory drug to inhibit cancer cells. This was considering previous reports in the literature that revealed the anticancer activity of naproxen derivatives.[71] The loading of NAP on the surface of Fe₃O₄@CDs more possibly occurs by interactions between the functional groups on both naproxen and Fe₃O₄@CDs surface. Such interaction likely influenced the observed enhancement in the anticancer activity. Furthermore, the magnetic nanoparticles coated with methionine and PEG were similarly used to deliver naproxen to cancer cells (MDA-MB-231 and MCF-7) with obvious enhanced anticancer activity.[72] Therefore, the easily synthesized Fe₃O₄@CDs showed good performance not only as non-toxic staining agents, but also in delivering naproxen well to cell target and upgrading the effectiveness of HeLa cancer cell inhibition. This finding further opens the potency on MNP utilization for developing improved cancer disease treatment.[73]

Confocal investigation

Confocal laser scanning microscopy (CLSM) investigation was next conducted to observe the capability of Fe₃O₄@CDs in targeting HeLa cancer cells. This aspect is important to elaborate the possibility of the nanohybrid for effective naproxen delivery to the targeted cell. Moreover, the CLSM is good data to prove the potential application of Fe₃O₄@CDs acting as staining agents on the cancer cell. From Fig. S4 (ESI†), it is clear to that HeLa cells show green fluorescence after 1 h incubation with Fe₃O₄@CDs. By adding DAPI for particular nucleus cell staining, it confirmed the nanohybrid converge on the cytoplasm area of the cell. The nanohybrid transport and its insertion to

the cell was mediated by physical interactions, mainly hydrogen bonding and electrostatic interaction with the cell membrane, allowing the existence of the nanohybrid on the cytoplasm as the final target.[74] This CLSM result is quite clear to detecting the CDs' emission on the cell indicating role of CDs on the nanohybrid can work well.

NAP release evaluation

The releasing properties of the nanohybrid in naproxen delivery need to be improved for targeted delivery in clinical applications. The drug release profile was characterized by a dissolution test under adjusted conditions. The pH of the release medium also affected the amount of NAP released, as shown in Fig. 8. At pH = 7, 1.56% of the NAP was released after 360 min; this value decreased at pH = 9 and 4 to 1.48% and 1.33%, respectively. After 1440 min, the total released NAP at pH = 7, 9, and 4 were 1.66%, 1.47% and 1.36%, respectively. This pH-
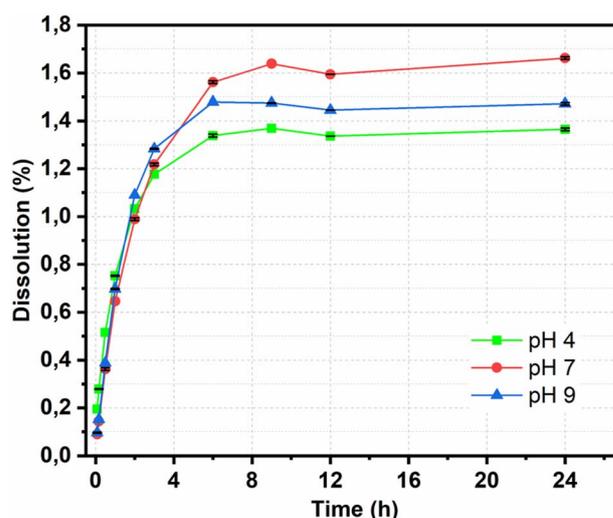

Fig. 8 Dissolution of Fe₃O₄@CDs nanohybrids at different pH values. All data are expressed as mean ± SD, $n = 3$.
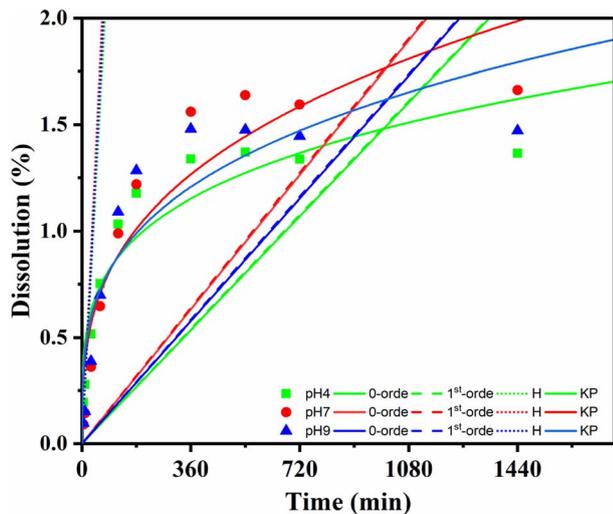
Fig. 9 Kinetic release of NAP from Fe_3O_4@CDs at varied pH (pH 4: green; pH 7: red; pH 9: blue) and compared to the 0-order; 1st-order, Higuchi (H), and Korsmeyer–Peppas (KP) models.

dependent response was potentially due to the improved electrostatic attraction of CDs. A slightly basic medium can well dissolve NAP; remarkably, CDs contain plentiful high-power moieties (*i.e.*, hydroxyl and carboxyl functional groups) that can provide an electronegative charge. This induced the electronegative charge that can prompt high electrostatic aversion. In depth, dissolution data of Fe_3O_4@CDs-NAP at different pH values were also compared with common drug release patterns, such as zero-order, first-order, Higuchi, and Korsmeyer–Peppas kinetics models (Fig. 9). The obtained drug data closely followed the Korsmeyer–Peppas kinetics pattern (see on Table S2†). The model describes the releasing model of the drug from a polymeric material or any material with an organized structure;[64] this finding indicates that naproxen release is influenced by Fe_3O_4@CDs. The graphene-like structure that existed on CDs and Fe_3O_4 crystal maybe detected as an organized structure that has effects naproxen's motion. In this kinetics model, the diffusion exponent (n) defines the influence drug release mechanism. When $n \leq 0.45$, the drug release mechanism can be described by the Fickian diffusion; $0.45 < n < 0.89$ corresponds to a non-Fickian transport mechanism, $n = 0.89$ corresponds to case II (relaxational) transport, and $n > 0.89$ corresponds to a super case II transport mechanism.[75,76] The resulting diffusion exponent (n) at pH = 4, 7 and 9 was 0.2 464 037, 0.3 252 665 and 0.2 858 769, respectively, indicating that the drug release mechanism followed the Fickian diffusion.

Conclusion

Nanohybrid Fe_3O_4 coated with CDs has been successfully synthesized and characterized in the present study. The characterization results validated the structure of Fe_3O_4 as well as CDs surrounding it; it was confirmed that each component maintained its functionalities. The obtained Fe_3O_4@CD nanohybrid gives a high QY; meanwhile, it still also maintains its magnetic properties. The CA

has been proven to stabilize magnetite, and also showed a decreased size diameter of the nanohybrid on Fe_3O_4@CDs. The cytotoxicity experiment demonstrated that the nanohybrid was non-toxic and allowed naproxen to be delivered specifically to HeLa cells. The developed nanohybrid also demonstrated pH-dependent NAP release that followed the Korsmeyer–Peppas kinetics model. This finding on multi-tasking nanohybrid refers to an integrative way on cancer treatment clinically.

Conflicts of interest

The authors declare that no known competing financial interests or personal relationships influence the work on this paper.

Abbreviations

Magnetic nanoparticles	(MNPs)
Carbon dots	(CDs)
Quantum yield	(QY)
Magnetite	(Fe_3O_4)
Citric acid	(CA)
Naproxen	(NAP)
Computer tomography	(CT)
Magnetic resonance imaging	(MRI)
Deionised	(DI)
CA-coated Fe_3O_4	(Fe_3O_4@CA)
Photoluminescence	(PL)
Nanohybrid Fe_3O_4 CDs	(Fe_3O_4@CDs)
NAP-loaded Fe_3O_4@CDs	(Fe_3O_4@CDs-NAP)
Ultraviolet-visible spectrophotometry	(UV-vis)
Fourier-transform infrared spectroscopy	(FTIR)
Atomic force microscopy	(AFM)
Dynamic light scattering	(DLS)
X-ray diffraction	(XRD)
Enzyme-linked immunosorbent assay	(ELISA)
Vibrating-sample magnetometer	(VSM)
Cell Counting Kit-8	(CCK-8)
Dimethyl sulfoxide	(DMSO)
Sodium hydroxide	(NaOH)
Ethanol	(C_2H_5OH)
Dulbecco's modified Eagle's medium	(DMEM)
Cytotoxic concentration	(CC50)
Inhibitory concentration	(IC50)
Rhodamine 6G	(R6G)

Acknowledgements

References

1 Y. Huang, L. Li, D. Zhang, L. Gan, P. Zhao, Y. Zhang, Q. Zhang, M. Hua and C. Jia, *Magn. Reson. Imaging*, 2020, **68**, 113–120.

2 M. Zhang, W. Wang, Y. Cui, N. Zhou and J. Shen, *Int. J. Nanomed.*, 2018, **13**, 2803.

3 J. Shan, L. Wang, H. Yu, J. Ji, W. Amer, Y. Chen, G. Jing, H. Khalid, M. Akram and N. Abbasi, *Mater. Sci. Technol.*, 2016, **32**, 602–614.

4 B. Li, X. Wang, Y. Guo, A. Iqbal, Y. Dong, W. Li, W. Liu, W. Qin, S. Chen and X. Zhou, *Dalton Trans.*, 2016, **45**, 5484–5491.

5 F. Zhu, D. Li, Q. Ding, C. Lei, L. Ren, X. Ding and X. Sun, *Biosens. Bioelectron.*, 2020, **147**, 111787.

6 S. M. Fotukian, A. Barati, M. Soleymani and A. M. Alizadeh, *J. Alloys Compd.*, 2020, **816**, 152548.

7 D. H. Kim, D. W. Kim, J. Y. Jang, N. Lee, Y.-J. Ko, S. M. Lee, H. J. Kim, K. Na and S. U. Son, *ACS Appl. Mater. Interfaces*, 2020, **12**, 37628–37636.

8 S. Sadighian, N. Bayat, S. Najaflou, M. Kermanian and M. Hamidi, *ChemistrySelect*, 2021, **6**, 2862–2868.

9 Y. Zhang, X. Li, Y. Zhang, J. Wei, W. Wang, C.-Z. Dong, Y. Xue, M. Liu and R. Pei, *New J. Chem.*, 2021, **45**, 7918–7941.

10 B. Maleki, H. Alinezhad, H. Atharifar, R. Tayebee and A. V. Mofrad, *Org. Prep. Proced. Int.*, 2019, **51**, 301–309.

11 N. B. Dewage, A. S. Liyanage, C. U. Pittman Jr, D. Mohan and T. Mlsna, *Bioresour. Technol.*, 2018, **263**, 258–265.

12 E. Kim, K. Lee, Y.-M. Huh and S. Haam, *J. Mater. Chem. B*, 2013, **1**, 729–739.

13 T. Kang, F. Li, S. Baik, W. Shao, D. Ling and T. Hyeon, *Biomaterials*, 2017, **136**, 98–114.

14 A. Jesus, J. Jesus, R. Lima, K. Moura, J. Almeida, J. Duque and C. Meneses, *Ceram. Int.*, 2020, **46**, 11149–11153.

15 F. Zhan, R. Wang, J. Yin, Z. Han, L. Zhang, T. Jiao, J. Zhou, L. Zhang and Q. Peng, *RSC Adv.*, 2019, **9**, 878–883.

16 C. Li, Y. Fu, Z. Wu, J. Xia and X. Wang, *Nanoscale*, 2019, **11**, 12997–13006.

17 D. Liu, J. Lai, R. Wang, L. Ye and Y. Tian, *ACS Biomater. Sci. Eng.*, 2019, **5**, 6196–6206.

18 P. Hu, T. Chang, W.-J. Chen, J. Deng, S.-L. Li, Y.-G. Zuo, L. Kang, F. Yang, M. Hostetter and A. A. Volinsky, *J. Alloys Compd.*, 2019, **773**, 605–611.

19 H. Veisi, M. Ghorbani and S. Hemmati, *Mater. Sci. Eng., C*, 2019, **98**, 584–593.

20 M. O. Besenhard, A. P. LaGrow, S. Famiani, M. Pucciarelli, P. Lettieri, N. T. K. Thanh and A. Gavriilidis, *React. Chem. Eng.*, 2020, **5**, 1474–1483.

21 H. Sadegh, H. Helmi, A. S. Hamdy, A. Masjedi, M. J. H. Dastjerdi and R. Shahryari-ghoshekandi, *Chem. Adv. Mater.*, 2016, **1**, 1–12.

22 J.-F. Lin, C.-C. Tsai and M.-Z. Lee, *J. Magn. Magn. Mater.*, 2014, **372**, 147–158.

23 X. Liu, C. Chen, Y. Zhao and B. Jia, *J. Nanomater.*, 2013, **34**, 1–7.

24 W. Ling, M. Wang, C. Xiong, D. Xie, Q. Chen, X. Chu, X. Qiu, Y. Li and X. Xiao, *J. Mater. Res.*, 2019, **34**, 1828–1844.

25 J. A. Barreto, W. O'Malley, M. Kubeil, B. Graham, H. Stephan and L. Spiccia, *Adv. Mater.*, 2011, **23**, 18–40.

26 Z. Xie, F. Wang and C. y. Liu, *Adv. Mater.*, 2012, **24**, 1716–1721.

27 J. Nam, N. Won, J. Bang, H. Jin, J. Park, S. Jung, S. Jung, Y. Park and S. Kim, *Adv. Drug Delivery Rev.*, 2013, **65**, 622–648.

28 S. F. A. Sugito, F. Firdaus, Y. Aung, S. C. W. Sakti, H.-T. Chiu and M. Z. Fahmi, *J. Mater. Res.*, 2022, 1–11.

29 Z. Zhang, G. Yi, P. Li, X. Zhang, H. Fan, Y. Zhang, X. Wang and C. Zhang, *Nanoscale*, 2020, **12**, 13899–13906.

30 D. Xu, F. Lei, H. Chen, L. Yin, Y. Shi and J. Xie, *RSC Adv.*, 2019, **9**, 8290–8299.

31 A. Wibrianto, S. Q. Khairunisa, S. C. Sakti, Y. L. Ni'mah, B. Purwanto and M. Z. Fahmi, *RSC Adv.*, 2021, **11**, 1098–1108.

32 K. Hola, Y. Zhang, Y. Wang, E. P. Giannelis, R. Zboril and A. L. Rogach, *Nano Today*, 2014, **9**, 590–603.

33 S. Kang, Y. K. Jeong, J. H. Ryu, Y. Son, W. R. Kim, B. Lee, K. H. Jung and K. M. Kim, *Appl. Surf. Sci.*, 2020, **506**, 144998.

34 M. Ali, R. Riaz, A. S. Anjum, K. C. Sun, H. Li, S. Ahn, S. H. Jeong and M. J. Ko, *J. Colloid Interface Sci.*, 2021, **586**, 349–361.

35 M. Z. Fahmi, J. K. Chen, C. C. Huang, Y. C. Ling and J.-Y. Chang, *J. Mater. Chem. B*, 2015, **3**, 5532–5543.

36 M. Ashrafizadeh, R. Mohammadinejad, S. K. Kailasa, Z. Ahmadi, E. G. Afshar and A. Pardakhty, *Adv. Colloid Interface Sci.*, 2020, **278**, 102123.

37 D. Dey, T. Bhattacharya, B. Majumdar, S. Mandani, B. Sharma and T. K. Sarma, *Dalton Trans.*, 2013, **42**, 13821–13825.

38 M. Zheng, Z. Xie, D. Qu, D. Li, P. Du, X. Jing and Z. Sun, *ACS Appl. Mater. Interfaces*, 2013, **5**, 13242–13247.

39 Y. Lin, B. Yao, T. Huang, S. Zhang, X. Cao and W. Weng, *Microchim. Acta*, 2016, **183**, 2221–2227.

40 S. K. Kailasa and J. R. Koduru, *Trends Environ. Anal. Chem.*, 2022, **33**, e00153.

41 M. Z. Fahmi, K.-L. Ou, J.-K. Chen, M.-H. Ho, S.-H. Tzing and J.-Y. Chang, *RSC Adv.*, 2014, **4**, 32762–32772.

42 S. P. Singh, *J. Biomed. Nanotechnol.*, 2011, **7**, 95–97.

43 X. Ren, H. Chen, V. Yang and D. Sun, *Front. Chem. Sci. Eng.*, 2014, **8**, 253–264.

44 J. Xie, G. Liu, H. S. Eden, H. Ai and X. Chen, *Acc. Chem. Res.*, 2011, **44**, 883–892.

45 N. Kaur, P. Tiwari, Z. Abbas and S. M. Mobin, *J. Mater. Chem. B*, 2022, **10**, 5251–5262.

46 J. Cheng, R. Xia, H. Li, Z. Chen, X. Zhou, X. Ren, H. Dong, R. Lin and J. Zhou, *ACS Sustainable Chem. Eng.*, 2022, **10**, 3935–3950.

47 X. Lin, Y. Mei, C. He, Y. Luo, M. Yang, Y. Kuang, X. Ma, H. Zhang and Q. Huang, *Front. Chem.*, 2021, **9**, 1–8.

48 Y. Hu, P. Wang, C. E. Bunker, L. R. Teisl, M. Reibold, S. Yan, H. Qian, D. He and Y.-P. Sun, *RSC Adv.*, 2017, 7, 41304–41310.

49 W. Purnamasari, T. A. Budiastanti, A. Aminatun, U. Rahmah, S. Sumarsih, J.-Y. Chang and M. Z. Fahmi, *RSC Adv.*, 2022, **12**, 8019–8029.

50 S. Javanbakht, N. Nazari, R. Rakhshaei and H. Namazi, *Carbohydr. Polym.*, 2018, **195**, 453–459.

51 H. El Ghandoor, H. M. Zidan, M. M. H. Khalil and M. I. M. Ismail, *Int. J. Electrochem. Sci.*, 2012, **7**, 5734–5745.

52 M. Z. Fahmi, J.-K. Chen, C.-C. Huang, Y.-C. Ling and J.-Y. Chang, *J. Mater. Chem. B*, 2015, **3**, 5532–5543.

53 T. P. Armedya, M. F. Dzikri, S. C. W. Sakti, A. Abdulloh, Y. Raharjo, S. Wafiroh and M. Z. Fahmi, *J. Bionanosci.*, 2019, **9**, 274–284.

54 K. Lawson-wood, S. Upstone and K. Evans, in *Fluorescene Spectroscopy*, PerkinElmer Inc., Seer Green, UK, 2018.

55 M. A. Dheyab, A. A. Aziz, M. S. Jameel, O. A. Noqta, P. M. Khaniabadi and B. Mehrdel, *Sci. Rep.*, 2020, **10**, 1–8.

56 R. Jin, B. Lin, D. Li and H. Ai, *Curr. Opin. Pharmacol.*, 2014, **18**, 18–27.

57 C. Li, Z. Li, X. Ye, X. Yang, G. Zhang and Z. Li, *Chem. Eng. J.*, 2018, **334**, 1614–1620.

58 Y. Tu, F. Peng, P. B. White and D. A. Wilson, *Angew. Chem., Int. Ed.*, 2017, **56**, 7620–7624.

59 W. J. Zhang, C. Y. Hong and C. Y. Pan, *Macromol. Rapid Commun.*, 2019, **40**, 1800279.

60 Y. Wen, M. Xu, X. Liu, X. Jin, J. Kang, D. Xu, H. Sang, P. Gao, X. Chen and L. Zhao, *Colloids Surf., B*, 2019, **173**, 842–850.

61 N. Tejwan, A. K. Saini, A. Sharma, T. A. Singh, N. Kumar and J. Das, *J. Controlled Release*, 2021, **330**, 132–150.

62 N. Murugan and A. K. Sundramoorthy, *New J. Chem.*, 2018, **42**, 13297–13307.

63 N. Murugan, M. Prakash, M. Jayakumar, A. Sundaramurthy and A. K. Sundramoorthy, *Appl. Surf. Sci.*, 2019, **476**, 468–480.

64 M. Z. Fahmi, R. A. Prasetya, M. F. Dzikri, S. C. W. Sakti and B. Yuliarto, *Mater. Chem. Phys.*, 2020, **250**, 123055.

65 G. Supriyanto, N. K. Rukman, A. K. Nisa, M. Jannatin, B. Piere, A. Abdullah, M. Z. Fahmi and H. S. Kusuma, *BioResources*, 2018, **13**, 4832–4840.

66 T. Espinosa-Ortega, I. Luk'yanchuk and Y. Rubo, *Phys. Rev. B: Condens. Matter Mater. Phys.*, 2013, **87**, 205434.

67 F. Zhang, F.-G. Zhang, S.-Q. Liu, J. Meng, H.-L. Miao and W. Jiang, *Chin. J. Phys.*, 2020, **66**, 390–400.

68 M. Havrdova, K. Hola, J. Skopalik, K. Tomankova, M. Petr, K. Cepe, K. Polakova, J. Tucek, A. B. Bourlinos and R. Zboril, *Carbon*, 2016, **99**, 238–248.

69 M. Z. Fahmi and J.-Y. Chang, *RSC Adv.*, 2014, **4**, 56713–56721.

70 E. ÇETİN, Y. D. ARACAGÖK, H. GÖKER, M. A. ONUR and N. CİHANGİR, *Hacettepe Journal of Biology and Chemistry*, 2021, **49**, 25–36.

71 M. M. Alam, S. Nazreen, A. S. Almalki, A. A. Elhenawy, N. I. Alsenani, S. E. I. Elbehairi, A. M. Malebari, M. Y. Alfaifi, M. A. Alsharif and S. Y. Alfaifi, *Pharmaceuticals*, 2021, **14**, 870.

72 F. E. Yeganeh, A. E. Yeganeh, M. Yousefi, B. Farasati Far, I. Akbarzadeh, D. O. Bokov, K. Raahemifar and M. Soltani, *Cancers*, 2022, **14**, 1797.

73 M. Z. Fahmi, W. Sukmayani, S. Q. Khairunisa, A. M. Witaningrum, D. W. Indriati, M. Q. Y. Matondang, J. Y. Chang, T. Kotaki and M. Kameoka, *RSC Adv.*, 2016, **6**, 92996–93002.

74 B. Li, X. Wang, Y. Guo, A. Iqbal, Y. Dong, W. Li, W. Liu, W. Qin, S. Chen, X. Zhou and Y. Yang, *Dalton Trans.*, 2016, **45**, 5484–5491.

75 G. Yadav, M. Bansal, N. Thakur, S. Khare and P. Khare, *J. Sci. Res.*, 2013, **16**, 782–795.

76 M. Z. Fahmi, N. F. Sholihah, A. Wibrianto, S. C. Sakti, F. Firdaus and J.-y. Chang, *Mater. Chem. Phys.*, 2021, **267**, 124596.